AGU ADVANCING EARTH AND SPACE SCIENCE

Earth and Space Science

RESEARCH ARTICLE
10.1029/2020EA001447

Special Section:
Results from 10 Years of UAVSAR Observations

A Computationally Efficient Hybrid Framework for Polarimetric Calibration of Quad-Pol SAR Data

Abhisek Maiti[1,2], Shashi Kumar[2], Valentyn Tolpekin[3], and Shefali Agarwal[2]

[1]Faculty ITC, University of Twente, Enschede, The Netherlands, [2]Indian Institute of Remote Sensing, ISRO, Dehradun, India, [3]ICEYE, Espoo, Finland

Key Points:

- A computationally efficient algorithm for Polarimetric Synthetic Aperture Radar (PolSAR) calibration
- Estimation and comparison of PolSAR data quality before and after the calibration
- Comparison of existing PolSAR calibration algorithms

Correspondence to:
A. Maiti,
a.maiti@utwente.nl

Citation:
Maiti, A., Kumar, S., Tolpekin, V., & Agarwal, S. (2021). A computationally efficient hybrid framework for polarimetric calibration of quad-pol SAR data. *Earth and Space Science*, *8*, e2020EA001447. https://doi.org/10.1029/2020EA001447

Received 5 SEP 2020
Accepted 19 DEC 2020

Abstract Polarimetric Synthetic Aperture Radar (PolSAR) calibration is an essential preprocessing step that must be performed to ensure that the data quality is adequate. This, in turn, helps to minimize the propagation of errors in any further data processing or information extraction. Crosstalk and channel imbalance are two major distortions found to be present in the uncalibrated polarimetric SAR data. The PolSAR calibration mainly aims to reduce these two distortions revealing the true scattering pattern of the targets. In this regard, Quegan's algorithm and Ainsworth algorithm are two widely used algorithms for the PolSAR calibration. In this study, the accuracy and efficiency of these two algorithms have been thoroughly compared using suitable metrics. It has been shown that the Ainsworth algorithm performs better than Quegan's in terms of accuracy at the cost of poor computational efficiency. The data quality metrics also highlight the better calibration accuracy of the Ainsworth algorithm. The issue of higher computational complexity has been effectively addressed by coupling both of these algorithms. Evidently, the computational cost has been reduced in the case of the proposed algorithm. The polarization orientation angle (POA) shift is another distortion caused by the topographic variations present in the target scene. Therefore, correction of POA shift has been incorporated in this research by coupling it with the PolSAR calibration. Subsequently, the improvement in the scattering has been observed. In essence, the proposed algorithm coupled with the correction of POA shift rectifies the major polarimetric distortions with adequate accuracy and computational efficiency.

1. Introduction

Synthetic Aperture Radar (SAR) being a prominent remote sensing instrument having all-weather, day-and-night imaging capability, has gained unprecedented popularity in the recent trends of remote sensing. In addition, the polarimetric information in SAR data can be used to retrieve the geomorphological properties such as soil moisture and surface roughness (Skriver et al., 2003). SAR is an active microwave remote sensing system which transmits polarized microwave pulse and measures the power of the backscattered signal from the target in the form of complex values (Moreira et al., 2013). The radar observation of each pixel is the coherent sum of the backscatter response from all the distributed targets within the spatial extent of that pixel (Doring et al., 2011). These measurements represent the geophysical and geometric properties of the corresponding targets. Also, the radar measurement of a specific target must be consistent irrespective of the sensors, given that the influences of other factors (frequency of the radar, viewing geometry, and so on) on the radar observation are compensated. In this regard, the calibration of SAR data is a mandatory pre-processing step to ensure data quality.

The polarization for a plane electromagnetic (EM) wave is done to forcefully orient the electric field vector toward one pole based on the propagation axis, thereby creating an ellipse in each and every cycle (known as polarization ellipse). Upon interacting with the Earth's surface, the EM wave gets its polarization broken into different components (mainly due to the surface roughness): most portion vibrates in horizontal direction, some in vertical portion, and the rest remains unpolarized vibrating in all possible directions. The angle by which the polarization ellipse is mounted on its propagation axis is called polarization orientation angle (POA). The shape, size, structure, and orientation of features cause a shift in POA, which strongly influences the coherency matrix elements except for the first element (T_{11}) and imaginary components (Shukla & Kumar, 2018). Double bounce scattering (T_{22}) and volume scattering (T_{33}) are underestimated and overestimated respectively due to the POA shift (Lee & Ainsworth, 2011; Shukla & Kumar, 2018). Thus, it

is always recommended to compensate this de-orientation effect for reliable inferences to the model-based decomposition outputs like scattering property retrieval.

The ambiguities of the transmit-receive modules (TRMs) and other antenna elements make the horizontal component more sensitive to the vertical polarization (and vice-versa), thereby inducing crosstalk errors. These errors relatively contribute to an increased magnitude of cross-pol images resulting in overestimation of volume scattering properties (Chang et al., 2018). In addition, the amplitude or phase unconformity of different polarization channels cause imbalance in the transmission or reception of antenna gain (Babu et al., 2019). Coming to the influence of imbalance on the PolSAR images, there are two categories: (a) co-pol channel imbalance and (b) cross-pol channel imbalance. The former causes the distortion between the HH and VV channels whereas the later causes the distortion between HV and VH channels, thereby resulting in the deformation of scattering reciprocity (Chang et al., 2018). Furthermore, the polarization plane of the EM wave is rotated about the radar line of sight due to the presence of an external magnetic field caused by charged particles in the ionosphere of the Earth's atmosphere. Such changes in the polarization state lead to Faraday rotation error. Because of this, it can be observed that there are ambiguities and induced errors in the band ratio of different channels. The performance of target detection algorithms and polarization characteristics show insensitive results when the isolation is less than −30 dB and the amplitude imbalance is larger than −0.6 dB (Liu et al., 2016).

In general, the term “calibration” refers to the process of establishing the relationship between the measurements and the actual quantities with the proper estimation of measurement uncertainties (Clifford, 1985). This definition is equally applicable for Polarimetric SAR (PolSAR) calibration. PolSAR generally refers to the fully polarimetric or quad-pol acquisition mode of SAR unless specified otherwise. Theoretically, different combinations of the polarization channels are known to be related to each other (Cloude, 2009). These relationships play pivotal roles in the retrieval of the geomorphological properties of the targets. Ideally, these relationships should be reflected in the corresponding measurements, however, in reality it has been observed that the measurements from the SAR sensor do not always hold these properties. There are several factors that corrupt the integrity of the PolSAR measurements (Freeman et al., 1992). The working principle of SAR dictates that the pixel spacing in the SAR image is smaller compared to the spatial resolution. Due to this reason, a typical point target occupies more than one pixel. This, in turn, leads to the error in the estimation of the Radar Cross Section (RCS; Van Zyl & Kim, 2011). In addition to this, The anomaly which hinders this comparability of measurements from different polarization channels is known as channel imbalance representing the imbalance both in amplitude and phase (Van Zyl & Kim, 2011). Moreover, The anomalies introduced in PolSAR data due to improper channel isolation are commonly known as crosstalk (Baffelli et al., 2018). According to Freeman et al. (1992), the sensor calibration alone cannot entirely avoid all these issues. Therefore, PolSAR data calibration as an additional pre-processing step is necessary to reduce the effects of these anomalies.

Calibration of PolSAR data is a reasonably complex process which is mostly based on the statistical comparison of the data with the ideal theoretical models assuming the backscattering symmetry (Al-kahachi, 2014). This typically involves several crucial steps (Fore et al., 2015). First, The antenna gain of the SAR sensor is appropriately estimated and the corresponding data set is corrected through the absolute radiometric calibration minimizing error in the estimation of the RCS (Fore et al., 2009). Along with this, the phase calibration reduces the phase imbalance and partially corrects the channel imbalance (Fore et al., 2009). Finally, the rectification of channel imbalance ensures the cross-pol reciprocity and the crosstalk minimization reduces the error in the data due to imperfect isolation of the polarization channels (Fore et al., 2015). In addition, correction for Faraday rotation is required for the spaceborne SAR platforms working in the lower frequency bands. Moreover, The variation in the topography affects the polarization state of the signal (Lee et al., 2000). This shift in the POA which should also be rectified (Lee et al., 2018).

There are well established theoretical models for radiometric correction and corresponding phase calibration (Doring et al., 2011; El-Darymli et al., 2014; Gray et al., 1990; Van Zyl & Kim, 2011). However, calibration techniques for crosstalk and channel imbalance minimization are still under active research. Currently, there are two widely popular methods for crosstalk calibration (Fore et al., 2015). The approach of Quegan (1994) is based upon the assumption of reciprocity of the cross polarized channels. In addition, it

also assumes azimuth symmetry, which means that the co-pol and cross-pol channels are truly uncorrelated in any scene dominated by distributed targets (Quegan, 1994). Kimura et al. (2004) further improved Quegan's algorithm by incorporating the cross-channel noise imbalance, this algorithm is popularly known as the improved Quegan's algorithm. However, the assumptions adopted by Quegan (1994) do not always hold in the raw SAR data set. Later on, Ainsworth et al. (2006) proposed a posteriori model to estimate the crosstalk which is only based upon the weak constraint of scattering reciprocity. In addition to this, Shimada (2011) proposed a decomposition model-based approach where polarization distortion matrix can be alliteratively calculated from a system of nonlinear equations. These Iterative algorithms are observed to provide a distortion matrix with minimal residual noise compared to noniterative algorithms like Quegan's algorithm (Fore et al., 2015). However, iterative algorithms are computationally expensive than noniterative algorithms due to their iterative nature (Fore et al., 2009).

In this study, an improved approach has been proposed to calibrate PolSAR data preserving the calibration accuracy of the iterative algorithm while optimizing the computational cost. The proposed approach combines both Quegan's algorithm and Ainsworth's algorithm and takes system noise into account. Moreover, correction of POA shift has been considered as an essential part of the PolSAR calibration itself instead of considering it as a separate process.

2. Proposed Method

In this study, the process of PolSAR calibration has been divided into three important sequential steps, namely, radiometric and phase calibration, crosstalk and channel imbalance calibration and POA shift correction. In case of spaceborne SAR data, the correction for Faraday rotation has to be performed along with the POA shift correction step.

2.1. Radiometric Calibration

Radiometric and phase calibrations are the crucial preceding steps of any polarimetric calibration (Fore et al., 2015). The phase calibration helps in minimizing the phase bias present in both co-pol channels and cross-pol channels whereas, the purpose of the radiometric correction is to correctly convert pixel values to corresponding normalized RCS (Freeman et al., 1992). Assuming that the correction for antenna pattern has already been applied and neglecting the crosstalk, the radiometric and phase calibration can be modeled as given in Equation 1a (Fore et al., 2009).

$$\begin{bmatrix} s'_{vv} & s'_{vh} \\ s'_{hv} & s'_{hh} \end{bmatrix} = A \begin{bmatrix} s_{vv} f^2 e^{i(\phi_{t,v}+\phi_{t,r})} & s_{vh}(f\ /\ g) e^{i\phi_{t,h}+\phi_{r,v}} \\ s_{hv} f g e^{i(\phi_{t,v}+\phi_{r,h})} & s_{hh} e^{i(\phi_{t,h}+\phi_{r,h})} \end{bmatrix} \tag{1a}$$

$$\mathrm{S}_{\tau} = \begin{bmatrix} s'_{vv} & s'_{vh} \\ s'_{hv} & s'_{hh} \end{bmatrix} \tag{1b}$$

$$\mathrm{S}_{o} = \begin{bmatrix} s_{vv} & s_{vh} \\ s_{hv} & s_{hh} \end{bmatrix} \tag{1c}$$

here, S_o is the uncalibrated scattering matrix, S_τ is radiometric, and phase calibrated scattering matrix. The notation s_{tr} represents the backscattering from transmitted polarization t and received polarization r. The term A is the absolute calibration parameter whereas f and g are co-pol and cross-pol channel imbalance parameters respectively. The notation $\phi_{x,y}$ represents phase error in polarization channel y, where x signifies whether it corresponds to transmission (t) or reception (r). There are well-established methods to estimate the unknown radiometric and phase calibration parameters in the Equation 1a. Fore et al. (2009) and Fore et al. (2015) provide the detailed methodology of such an approach.

2.2. Crosstalk and Channel Imbalance Calibration

The radiometric and phase calibrated SAR data are considered to be partially calibrated because the channel imbalance is not entirely minimized and crosstalk is still present in the data set. Crosstalk and channel imbalance are generally modeled using distortion matrix and the respective parameters are estimated from the covariance matrix of the radiometric and phase calibrated PolSAR data.

When we talk about channel balancing, our focus is to preserve the orthogonality of the signals in the co-pol and cross-pol channels i.e. the phase, amplitude, and delay differences need to be managed for precise measurements of the target properties (cf. pages 37–38, Section 3.1.5 of Doerry and Bickel [2018]). It is a system issue and needs to be dealt at the hardware scale. To be concise and clear, issues related to channel imbalances should not be an afterthought however should be incorporated during the hardware design. But in the situation, where the effects of residual channel imbalance are mitigated at later stages, we need to take care of it computationally by implementing data-driven techniques (cf. page 40, Section 4.3 of Doerry and Bickel [2018]).

On the other hand, the typical, and ideal, assumption is that each channel processes only its own desired input. That is, the output of channel k is not influenced by the signal in channel l. Of course, this is ideal, and we are never quite so fortunate. The ability of a signal in one channel to leak, or couple, to another channel is termed "cross-talk." As such, it can be considered a noise source that is highly correlated with a signal in another channel. Clearly, if signals in separate channels are expected to be orthogonal, cross-talk obviously diminishes that orthogonality" (cf. page 26, section 2.11.3 of Doerry and Bickel [2018]).

To conclude, these two errors are very interrelated but they occur due to different reasons and hence, need to be discussed separately before utilizing them in the calibration equation, as in the Equation (2).

Crosstalk and Channel Imbalance Model

According to Van Zyl and Kim (2011), the observed scattering matrix ($\mathbf{S}'_o$) can be modeled in terms of the true scattering matrix ($\mathbf{S}'_\tau$) and the respective distortion (D) as shown in the Equation 2a. Here, Y represents complex absolute calibration gain, u, v, w, z are the complex crosstalk parameters, and α, k are the complex channel imbalance parameters. The term n_{tr} represents the system noise of the backscattering from transmitted polarization t and received polarization r. System noise ($\mathbf{N}$) is extremely difficult to model and can be assumed to be negligible due to the appropriate sensor calibration.

$$\underbrace{\begin{bmatrix} s'_{hh} \\ s'_{vh} \\ s'_{hv} \\ s'_{vv} \end{bmatrix}}_{\mathbf{S}'_o} = Y \underbrace{\begin{bmatrix} 1 & w & v & vw \\ u & 1 & uv & v \\ z & wz & 1 & w \\ uz & z & u & 1 \end{bmatrix} \begin{bmatrix} \alpha k^2 & 0 & 0 & 0 \\ 0 & \alpha k & 0 & 0 \\ 0 & 0 & k & 0 \\ 0 & 0 & 0 & 1 \end{bmatrix}}_{\mathrm{D}} \underbrace{\begin{bmatrix} s_{hh} \\ s_{vh} \\ s_{hv} \\ s_{vv} \end{bmatrix}}_{\mathbf{S}'_\tau} + \underbrace{\begin{bmatrix} n_{hh} \\ n_{vh} \\ n_{hv} \\ n_{vv} \end{bmatrix}}_{\mathrm{N}} \tag{2a}$$

$$k = \frac{1}{\sqrt{\alpha}} \tag{2b}$$

Estimation of Covariance Matrix

Both Quegan's algorithm and Ainsworth's algorithm estimate the crosstalk and channel imbalance parameters from the covariance matrix. The polarimetric covariance matrix is computed from the vector form of the scattering matrix of fully polarimetric SAR data using Equation 3a and it has the form shown in Equation 3c where $\mathbf{S}$ in the Equation 3b represents the vector form of the scattering matrix (Fore et al., 2015). Assuming radiometric and phase calibration has already been applied to the data set, the channel imbalance parameters satisfy the Equation 2b (Fore et al., 2009).

$$\mathrm{C} = \left\langle \mathbf{S}\mathbf{S}^{\dagger} \right\rangle \tag{3a}$$

$$\mathbf{S} = [s_{hh}\ s_{vh}\ s_{hv}\ s_{vv}]^{\mathrm{T}} \tag{3b}$$

$$C_{i,j} = \left\langle S_i S_j^* \right\rangle : C_{i,j} \in \mathrm{C}, S_i \in \mathbf{S}\ \forall\ i,j \in \{1,2,3,4\} \tag{3c}$$

here, $\langle \bullet \rangle$ operator signifies the ensemble average operation. In this regard, the choice of kernel size in covariance matrix computation is crucial as it can affect the estimation of crosstalk parameters. Ideally, the kernel size should not be too large as the covariance may deviate from expected value due to the high variation in sizable spatial extent, on the other hand, it should not be too small as the correct estimation of covariance requires an adequate number of samples (pixels) to be present in the kernel.

Quegan's Algorithm

Quegan (1994) presented an approach to estimate the crosstalk and channel imbalance parameters provided the 2.2 are satisfied.

Quegan's Preconditions

1. The acquired data set is fully polarimetric and available in the form of the scattering matrix.
2. The observed scattering matrix can be modeled as a linear system
3. Scattering reciprocity is satisfied unless the target is physically altered
4. In the case of distributed targets, cross-polarized channels are not correlated
5. The off-diagonal terms of the distortion matrix are small compared to the diagonal terms

Accordingly, the crosstalk parameters can be estimated as shown in Equation (4). (Fore et al., 2009).

$$u = \left(C_{44}C_{21} - C_{41}C_{24}\right) / \Delta \tag{4a}$$

$$v = \left(C_{11}C_{24} - C_{21}C_{14}\right) / \Delta \tag{4b}$$

$$w = \left(C_{44}C_{31} - C_{41}C_{34}\right) / \Delta \tag{4c}$$

$$z = \left(C_{11}C_{34} - C_{31}C_{14}\right) / \Delta \tag{4d}$$

$$\Delta = C_{11}C_{44} - \left|C_{14}\right|^2 \tag{4e}$$

similarly, the channel imbalance parameter (α) can be derived as presented in Equations 5a–5f.

$$\alpha = \frac{\left|\alpha_1\alpha_2\right| - m^2 + \sqrt{\left(\left|\alpha_1\alpha_2\right| - m\right)^2 + 4m\left|\alpha_2\right|^2}}{2\left|\alpha_2\right|} \frac{\alpha_1}{\left|\alpha_1\right|} \tag{5a}$$

$$\alpha_1 = \left(C_{22} - uC_{12} - vC_{42}\right) / X \tag{5b}$$

$$\alpha_2 = X^* / \left(C_{33} - z^*C_{31} - w^*C_{34}\right) \tag{5c}$$

$$X = C_{32} - zC_{12} - wC_{42} \tag{5d}$$

$$m = n_{vh} / n_{hv} \tag{5e}$$

$$m \approx \left\langle s'_{vh}\, s'^*_{vh} \right\rangle / \left\langle s'_{vh} s'^*_{vh} \right\rangle \tag{5f}$$

Quegan (1994) assumed that the random noises in cross polarized channels are equal, that is $n_{vh} = n_{hv}$, thus, effectively $m = 1$. However, Kimura et al. (2004) showed that the parameter m can be estimated according to Equation 5f when Quegan's assumption regarding system noise in cross polarized channels is not satisfied, that is $n_{vh} \neq n_{hv}$.

Ainsworth's Algorithm

The assumptions of Quegan (1994) imply that the algorithm is only applicable when there is no POA, and the helicity is effectively zero (Ainsworth & Lee, 2001). These stringent requirements may not always be satisfied, there Ainsworth et al. (2006) proposed an new algorithm with comparatively less restrictive constraints. Ainsworth's algorithm follows a posterior approach and does not require prior relationship between the distortion during signal transmission and distortion during signal reception. Fore et al. (2015) showed that, Ainsworth's crosstalk parameters can be estimated from δ in Equation 6g, by solving the system of Equations 6a (Ainsworth et al., 2006). The initial value of channel imbalance parameter α can be estimated using the Equation 6h.

$$\begin{bmatrix} \Re(\zeta+\tau) & -\Im(\zeta-\tau) \\ \Im(\zeta+\tau) & \Re(\zeta-\tau) \end{bmatrix} \begin{bmatrix} \Re(\delta) \\ \Im(\delta) \end{bmatrix} = \begin{bmatrix} \Re(\chi) \\ \Im(\chi) \end{bmatrix} \tag{6a}$$

$$\zeta = \begin{bmatrix} 0 & 0 & C_{41} & C_{11} \\ C_{11} & C_{41} & 0 & 0 \\ 0 & 0 & C_{44} & C_{14} \\ C_{14} & C_{44} & 0 & 0 \end{bmatrix} \tag{6b}$$

$$\tau = \begin{bmatrix} 0 & C_{33} & C_{22} & 0 \\ 0 & C_{23} & C_{22} & 0 \\ C_{33} & 0 & 0 & C_{32} \\ C_{23} & 0 & 0 & C_{22} \end{bmatrix} \tag{6c}$$

$$\chi = \begin{bmatrix} C_{31} - A \\ C_{21} - A \\ C_{34} - B \\ C_{24} - B \end{bmatrix} \tag{6d}$$

$$A = \frac{1}{2}\left(C_{31} + C_{21}\right) \tag{6e}$$

$$B = \frac{1}{2}\left(C_{34} + C_{24}\right) \tag{6f}$$

$$\delta = \begin{bmatrix} u & v & w & z \end{bmatrix}^{\mathrm{T}} \tag{6g}$$

$$\alpha = \frac{C_{23}}{|C_{23}|}\sqrt{\left|\frac{C_{22}}{C_{33}}\right|} \tag{6h}$$

However, Ainsworth's algorithm is an iterative approach, therefore, in ith iteration calibrated covariance matrix (C_i) is derived from the previous covariance matrix (C_{i-1}) and the current distortion matrix (D_i) as shown in the Equation 7a.

$$\mathrm{C}_i = \Sigma_i \mathrm{C}_{i-1} \Sigma_i^{\dagger} \tag{7a}$$

$$\Sigma_i = \mathrm{D}_i^{-1} \tag{7b}$$

Accordingly, the crosstalk and channel imbalance parameters are adjusted using the Equations. 8a–8e. Here, u'_i, v'_i, w'_i, z'_i and α'_i are corresponding residual crosstalk and channel imbalance parameters at iteration i, estimated by solving the system of Equation 6a based on the current covariance matrix C_i.

$$u_i = u_{i-1} + u'_i \,/\, \sqrt{\alpha_{i-1}} \tag{8a}$$

$$v_i = v_{i-1} + v'_i \,/\, \sqrt{\alpha_{i-1}} \tag{8b}$$

$$w_i = w_{i-1} + w'_i \sqrt{\alpha_{i-1}} \tag{8c}$$

$$z_i = z_{i-1} + z'_i \sqrt{\alpha_{i-1}} \tag{8d}$$

$$\alpha_i = \alpha_{i-1}\alpha'_i \tag{8e}$$

Thus, the algorithm iteratively converges toward the solution until all crosstalk residuals are below the predecided precision threshold or the predecided maximum number of iterations has been reached.

Proposed Algorithm

Ainsworth's algorithm adopted by Fore et al. (2015) does not take into account the system noise. According to Ainsworth et al. (2006), the ideal covariance matrix (C_A) has the form shown in the equation. The term q in Equation 9c represents system noise therefore it depicts data quality as well. When $q > 1$, the covariance matrix is not positive definite. Therefore, crosstalk parameters cannot be calculated in these cases. The proposed algorithm takes this factor into account thus skips the calculation of the crosstalk parameters whenever $q > 1$, thus it reduces the overall error in the estimation of the crosstalk parameters.

$$\mathrm{C}_A = \begin{bmatrix} \sigma_{hhhh} & A^* & A^* & \sigma_{hhvv} \\ A & \beta & \beta' & B \\ A & \beta' & \beta & B \\ \sigma^*_{hhvv} & B^* & B^* & \sigma_{vvvv} \end{bmatrix} \tag{9a}$$

$$\eta = \beta - \beta' \tag{9b}$$

$$q = \eta \,/\, \beta \tag{9c}$$

Although the estimations of crosstalk parameters using Quegan's algorithm are no better than Ainsworth's algorithm, in some cases Quegan's crosstalk estimations are very close to the result of Ainsworth's algorithm (Fore et al., 2015). Therefore, in those cases, Ainsworth's iterative computations can be avoided by increasing the computational efficiency and saving execution time. Furthermore, in extreme cases, the crosstalk parameters may not converge to the expected precision within the maximum allowed iterations. In these cases, there is a possibility that estimations of Quegan's algorithm satisfy the residual threshold criteria rather than Ainsworth's estimations. The Proposed Algorithm takes care of this aspect as well.

Correction of Crosstalk and Channel Imbalance

The crosstalk and channel imbalance parameters vary with respect to range (Fore et al., 2009). However, Fore et al. (2015) showed that these parameters can also be scene dependent. Therefore, crosstalk and channel imbalance parameters should be averaged using a sliding window ignoring the anomalous pixels. Ideally, the sliding window should be narrower along the range compared to its width along the azimuth.

Algorithm: Proposed Algorithm by combining Quegan's and Ainsworth's algorithms (Maiti, 2019)

Input : Covariance matrix C_0, precision threshold ε and maximum allowed iterations i_{max}
Output: Crosstalk parameters u, v, w, z and channel imbalance parameter α

Estimate q from C_0 using equation (9c)
if $q < 1$
  Estimate u_Q, v_Q, w_Q, z_Q and α_Q from C_0 using Quegan's algorithm in eqs. (4a) to (4d) and (5a)
  Compute C_Q using equation (7a)
  Estimate δ_Q from C_Q by solving equation (6a)
  Set $\gamma_Q = \max(\hat{\delta}_Q) : \forall\ x \in \delta_q \Rightarrow |x| \in \hat{\delta}_Q)$
  if $\gamma_Q < \varepsilon$
    Accept Quegan's solution: $u = u_Q, v = v_Q, w = w_Q, z = z_Q$ and $\alpha = \alpha_Q$
  else
    Initialize $u_A = v_A = w_A = z_A = 0$j
    Compute channel imbalance parameter α_a using equation (6h)
    Set iteration count $i = 0$
    do
      Compute C_i using (7a)
      Estimate $\delta^{'}$ from C_i using equation (6a)
      Update u_A, v_A, w_A, z_A and α_A using eqs. (8a) to (8e)
      Set $\gamma_A = \max(\hat{\delta}_i) : \forall\ y \in \delta^{'} \Rightarrow |y| \in \hat{\delta}_i$
      $i = i + 1$
    while $\gamma_A > \varepsilon$ *and* $i < i_{max}$
    if $\gamma_A > \gamma_Q$
      Accept Quegan's solution: $u = u_Q, v = v_Q, w = w_Q, z = z_Q$ and $\alpha = \alpha_Q$
    else
      Accept Ainsworth's solution: $u = u_A, v = v_A, w = w_A, z = z_A$ and $\alpha = \alpha_A$
else
  Ignore crosstalk and channel imbalance estimation: $u = \mathrm{NaN}, v = \mathrm{NaN}, w = \mathrm{NaN}, z = \mathrm{NaN}, \alpha = \mathrm{NaN}$

Finally, for each pixel, the corrected scattering matrix S'_τ is obtained from the respective radiometric and phase calibrated scattering matrix S'_o and corresponding distortion matrix D using the Equation 10 ignoring the effect of system noise (**N**).

$$S'_\tau = D^{-1} S'_o \tag{10}$$

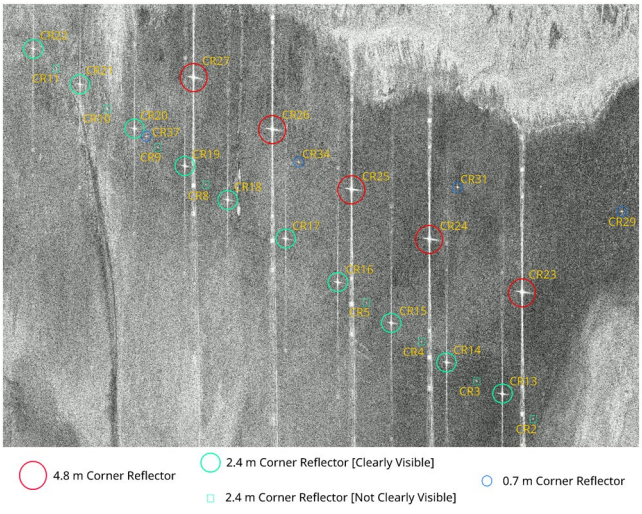

Figure 1. HH intensity image of the data set (see Table 1). The corner reflectors are marked according to their size and visibility. The southern region of the lake appears in the upper portion of the image because of the north to south flight track.

2.3. Calibration Evaluation Metrics

There are several metrics to measure the effects of the calibration on PolSAR data. Some of these metrics are extremely useful for analyzing the data quality and estimating the residual noise and uncertainty. The metrics used in this study to evaluate the calibration are discussed below.

Any change in the residual noise in the data should be reflected in the crosstalk and channel imbalance parameters estimated before and after performing calibration respectively. Moreover, according to Wang et al. (2011), the maximum normalized error (MNE) is a generalized metric to evaluate the proportion of noise present in the data. Furthermore, Villano and Papathanassiou (2013) suggested that the SNR of cross-pol channels of SAR data is crucial since the powers of the backscattered signal are comparatively very low with respect to backscatter powers of the co-pol channels.

In addition to these quantitative measures, the effect of calibration can be observed using a few qualitative measures also. In this regard, the

Table 1
Details of the Data Set

Attribute	Value
Date and time of acquisition	September 20, 2016, 22:31:22 UTC
Site	Rosamond, California, USA
Acquisition mode	Quad Pol
Flight line	35,012
Track ID	35
Average altitude	1.25 km
Look direction	Left
Frequency band	L (1.2575 GHz)
Radiometric calibration applied	Yes

roll invariant parameters can reveal the scattering pattern through the H-α plane and this scattering pattern can be compared with the expected scattering pattern of the scene Cloude (2009). The SAR decomposition models are also extremely useful for studying the scattering pattern. Sato et al. (2013) showed that the Y4R decomposition is highly reliable for the estimation of the true scattering pattern. Furthermore, the polarimetric signatures of the known targets such as corner reflectors can reveal the quality of PolSAR data when compared with the ideal theoretical response Cloude (2009). Polarimetric signatures are particularly useful to evaluate the radiometric and phase calibration Fore et al. (2015).

3. Study Area and Data Set

Rosamond dry lake is situated between Antelope Valley and the Mojave Desert in the southern part of California, United States of America. It is a naturally formed dry lake bed with a large flat surface of nearly 35 km^2 (Meyer & Bowers, 2012). The area is characterized by a hard surface having less than 40 cm of variation in curvature over a distance of 9 km and with the least amount of vegetation, thus making it suitable for a calibration validation (cal-val) site (Gibbs, 2017). At the southern part of the lake, an array of 38 triangular trihedral corner reflectors of

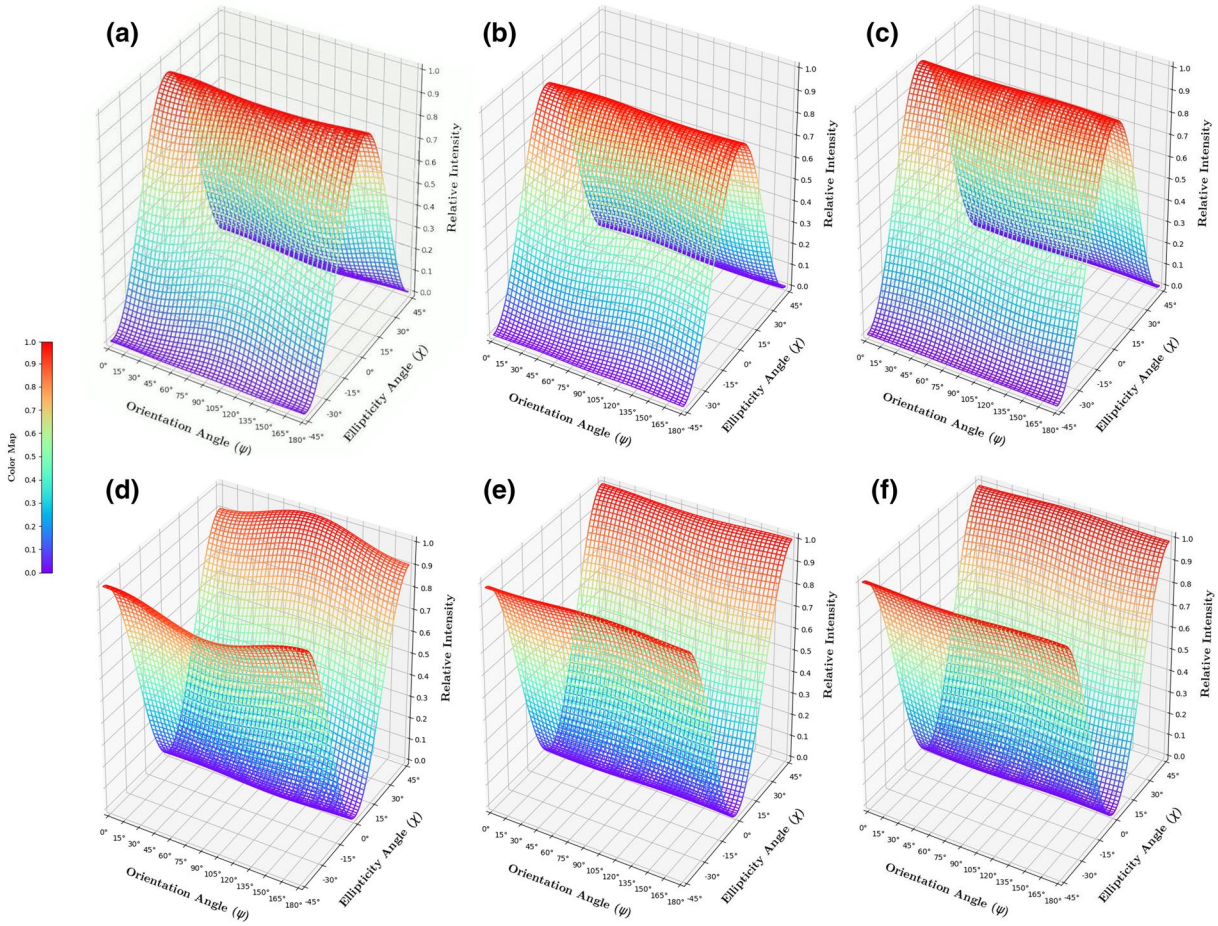

Figure 2. Polarimetric signatures of corner reflector 24. It is a triangular trihedral corner reflector with 4.8 m side length, co-pol signatures are shown in top row, cross-pol signatures are shown in the bottom row. Panels (a and d) are the signatures before calibration, (b and e) are signatures after calibration using Quegan' algorithm, (c and f) are the signatures after calibration using Ainsworth's algorithm.

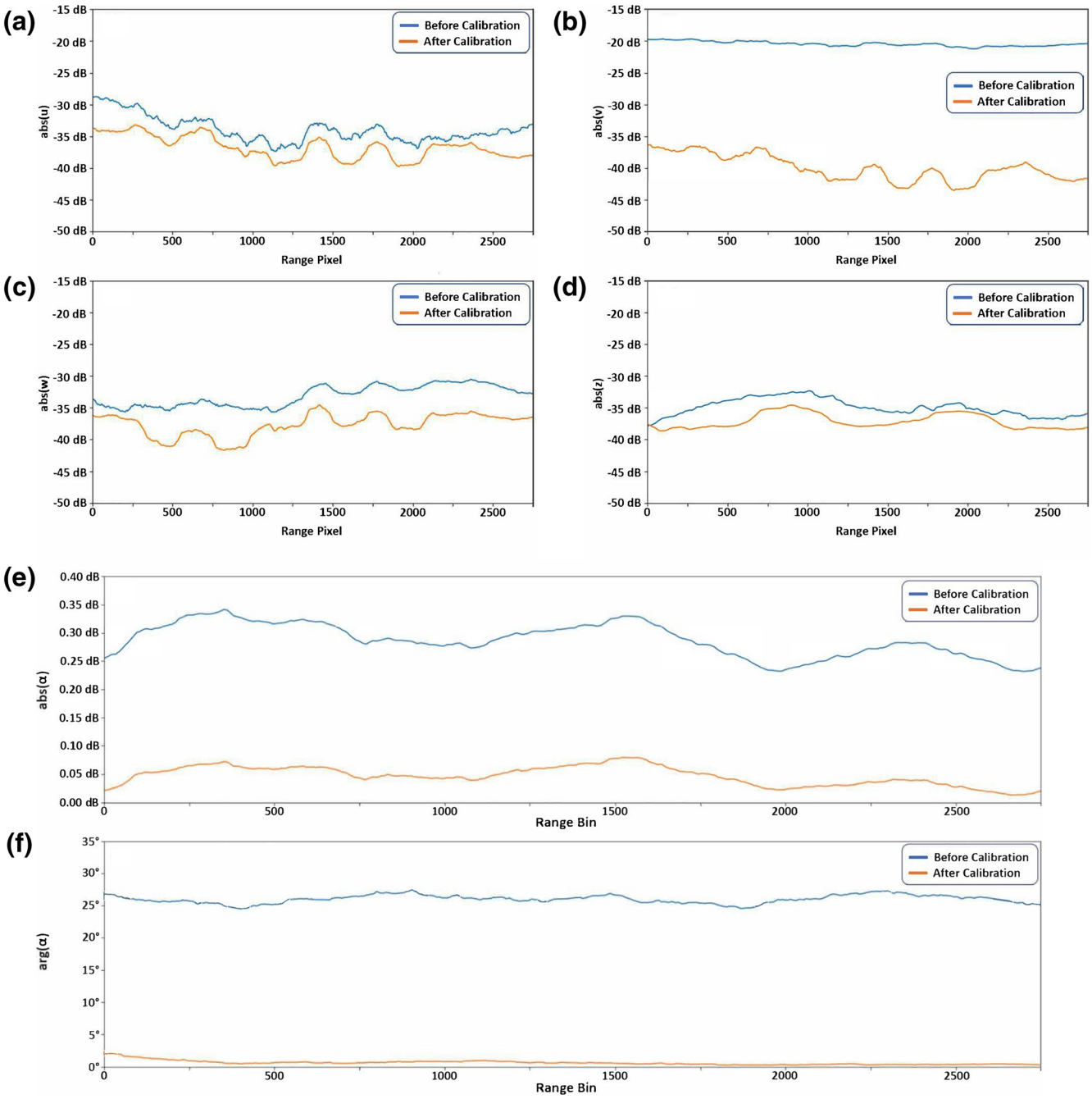

Figure 3. Variation of crosstalk and channel imbalance parameters estimated using Quegan's algorithm. The subfigures show the variation of the parameters as follows: (a) abs(u), (b) abs(v), (c) abs(w), (d) abs(z), (e) abs(α), (f) arg(α) All the crosstalk parameters and the channel imbalance parameter have reduced after performing calibration.

different sizes has been deployed and routinely maintained by NASA for the calibration of SAR instruments (Muellerschoen, 2018), as shown in Figure 1.

In this study, UAVSAR (Rosen et al., 2006) L band uncalibrated data set has been used. The slant range resolution of this data set is 1.8 m and the azimuth resolution is 0.8 m. Since the data set is only radiometrically calibrated, it is suitable for crosstalk calibration and POA shift correction. Since this is airborne SAR data, the correction for Faraday rotation is not applicable. The specified dataset is freely accessible from UAVSAR data repository (2020).

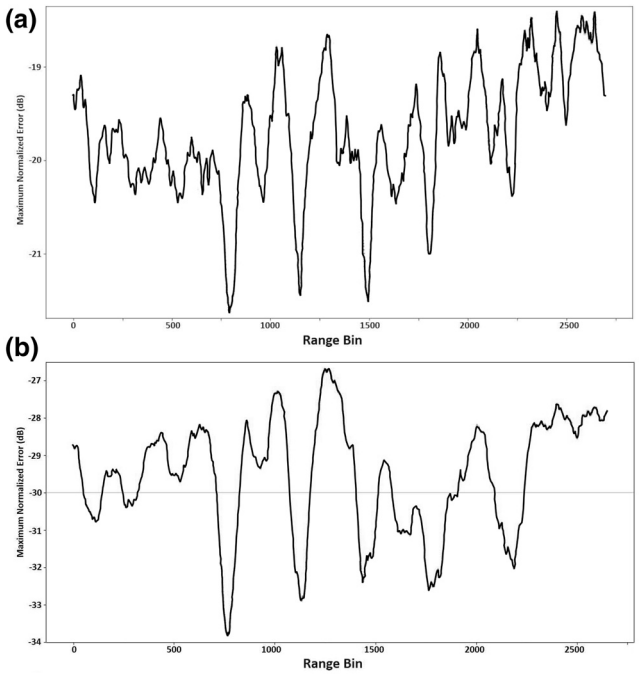

Figure 4. Variation of MNE with respect to the range direction (a) before Calibration, (b) after Quegan's calibration.

4. Results

The computation of the covariance matrix with adequate accuracy and precision is crucial for the correct estimation of the calibration parameters. However, the estimation of the covariance matrix depends upon the choice kernel size. In this study, all the covariance matrices have been computed using the 7×7 kernel. Furthermore, in each case, the cross-pol SNR has been estimated from a featureless area of 286×263 pixels with a 7×7 window. For the iterative crosstalk estimation algorithms, the maximum allowed iterations are set to be 16. Similar to the computation of the covariance matrix, the 7×7 window has been used for the estimation of POA shift.

4.1. Evaluation of Radiometric Calibration

The radiometric and phase calibration has already been applied in the data set. Therefore, the shapes of the polarimetric signatures at the corner reflector pixels should closely resemble the ideal shapes. The polarimetric signatures of CR24, a 4.8 m corner reflector is shown in the Figure 2. From Figures 2a and 2d it can be observed that, the response of this corner reflector closely depict the ideal shape of the triangular trihedral corner reflector. Although there are some visible distortions in the cross-pol signature, the distortions are not high, that is phase offset is reasonable. Therefore, it is safe to assume that the data set is radiometrically calibrated and the presence of phase imbalance is negligible.

4.2. Estimates of Quegan's Algorithm

The variations of crosstalk parameters estimated using Quegan's algorithm have been observed before and after the crosstalk calibration. In Figures 3a–3d, crosstalk parameters are plotted for the range direction over 2,750 range pixels. It can be observed that the parameter u varies roughly between -28 and -34 dB before the calibration and it varies roughly between -34 and -38 dB after the calibration. There are no anomalies in the estimation of u as the residual of u is less than the estimated u before the calibration in all the cases. The parameter v is estimated to be nearly -20 dB and it does not show many variations with respect to the range direction before the calibration. However, the residual of v varies between -35 and -43 dB and exhibits a similar pattern to that of residual u. The parameter w mostly varies around -35 dB before the calibration and it is estimated to be roughly between -35 and 42 dB after the calibration. The parameter z is estimated to be in the range of -34 to -36 dB before calibration and in the range of -35 to -39 dB after the calibration.

Similar to the crosstalk parameters, the estimated absolute value of channel imbalance parameter α and its phase is plotted against the range direction in Figures 3e and 3f respectively, both before and after the calibration. The amplitude of α varied between 0.25 and 0.35 dB before the calibration which reduced to below 0.07 dB after the calibration. On the other hand, the phase of α varied close to 27° before the calibration and it reduced to nearly 0° after performing the calibration. The residual amplitude and phase of α indicate that the channel imbalance has been substantially reduced.

Furthermore, the polarimetric signature of the corner reflector 24 after performing the crosstalk and channel imbalance calibration is shown in Figure 2. It is evident that the distortions present in Figure 2a and 2d have been significantly reduced in Figure 2b and 2d.

Accordingly, Figure 4a shows the variation of MNE before performing the crosstalk calibration. The MNE before performing the crosstalk varied between -18.41 dB and -21.63 dB. However, MNE has been reduced to the range of -26.69 to -33.81 dB after crosstalk calibration using Quegan's algorithm, as shown in Figure 4b. However, in Figure 4b it is also evident that a large number of range pixels do not satisfy the threshold of -30 dB.

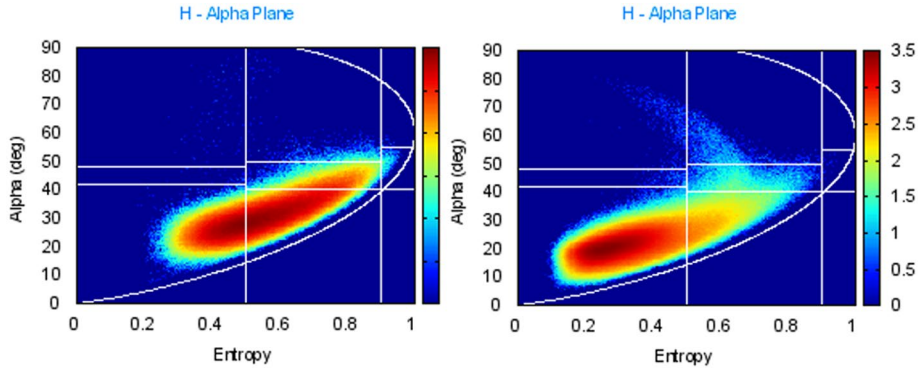

Figure 5. H-α Plane, (a) Before Crosstalk Calibration, (b) After calibration using Quegan's algorithm. Overall surface scattering has increased after calibration.

Similar to the MNE, the cross-pol SNR has been estimated before and after performing the crosstalk calibration which is shown in 5. In both cases, the histograms resemble a normal distribution. The mode of the histogram improved to 6.89 dB after the calibration from 6.12 dB before the calibration. However, the distribution of SNR is more uniform after the calibration compared to the distribution of the SNR before.

The study area for this research mostly comprises of a relatively smooth flat surface. Therefore, surface scattering is expected to be dominating. The volume scattering from vegetation might be present due to the presence of light vegetation near the edge of the dry lake bed. However, the volume scattering should be comparatively low. The H-α planes before and after the calibration are presented in Figure 5.

Figure 5a shows that most of the pixels lie in the region of surface scattering with low and medium entropy. However, a relatively large number of pixels depict medium entropy scattering rather than low entropy surface scattering. Furthermore, the pixel densities indicate that there is a significant amount of volume scattering present despite being lesser than the surface scattering. Presence of double bounce scattering, multiple scattering and anisotropic scattering is negligible. In contrast, the surface scattering in Figure 5b has significantly increased after performing the calibration using Quegan's algorithm. The amount of volume scattering has been reduced but still significantly present. However, the amount of double bounce scattering has increased which might be attributed to the rocky patches near the edge of the lake bed. In addition, the anisotropic scattering slightly increased which is unexpected as no anisotropic medium is known to be present in the study area.

4.3. Estimates of Ainsworth's Algorithm

The variation of crosstalk parameters in rage direction before and after the crosstalk calibration is shown in the Figures 6a–6d. Evidently, before calibration, in some cases, the crosstalk parameters are higher than the standard −35 dB threshold. However, all the crosstalk parameters have been reduced below −40 dB after the crosstalk calibration using Ainsworth's algorithm. Although the parameters u, w and z varied mostly below −45 dB, the parameter v gently varied between −40 and −45 dB. Furthermore, comparing Figures 3 and 6, it can be observed that the estimations of crosstalk parameters using Ainsworth's algorithm are relatively stable with respect to Quegan's algorithm.

The channel imbalance before and after performing Ainsworth crosstalk calibration is plotted with respect to range in the Figures 6e and 6f. The amplitude of α varied above 0.2 dB before the calibration which reduced below 0.05 dB after the calibration. The phase of α was stable around 26° before the calibration and it reduced to below 2° after performing the calibration. Unlike crosstalk parameters, the estimated value of α before the calibration shows a similar variation in the range direction to that of Quegan's estimation. The amplitude of α is lower after the calibration using Ainsworth's algorithm compared to the amplitude of α after performing calibration using Quegan's algorithm. However, the phase of α is more stable and lies closer to 0° in the case of Quegan's algorithm.

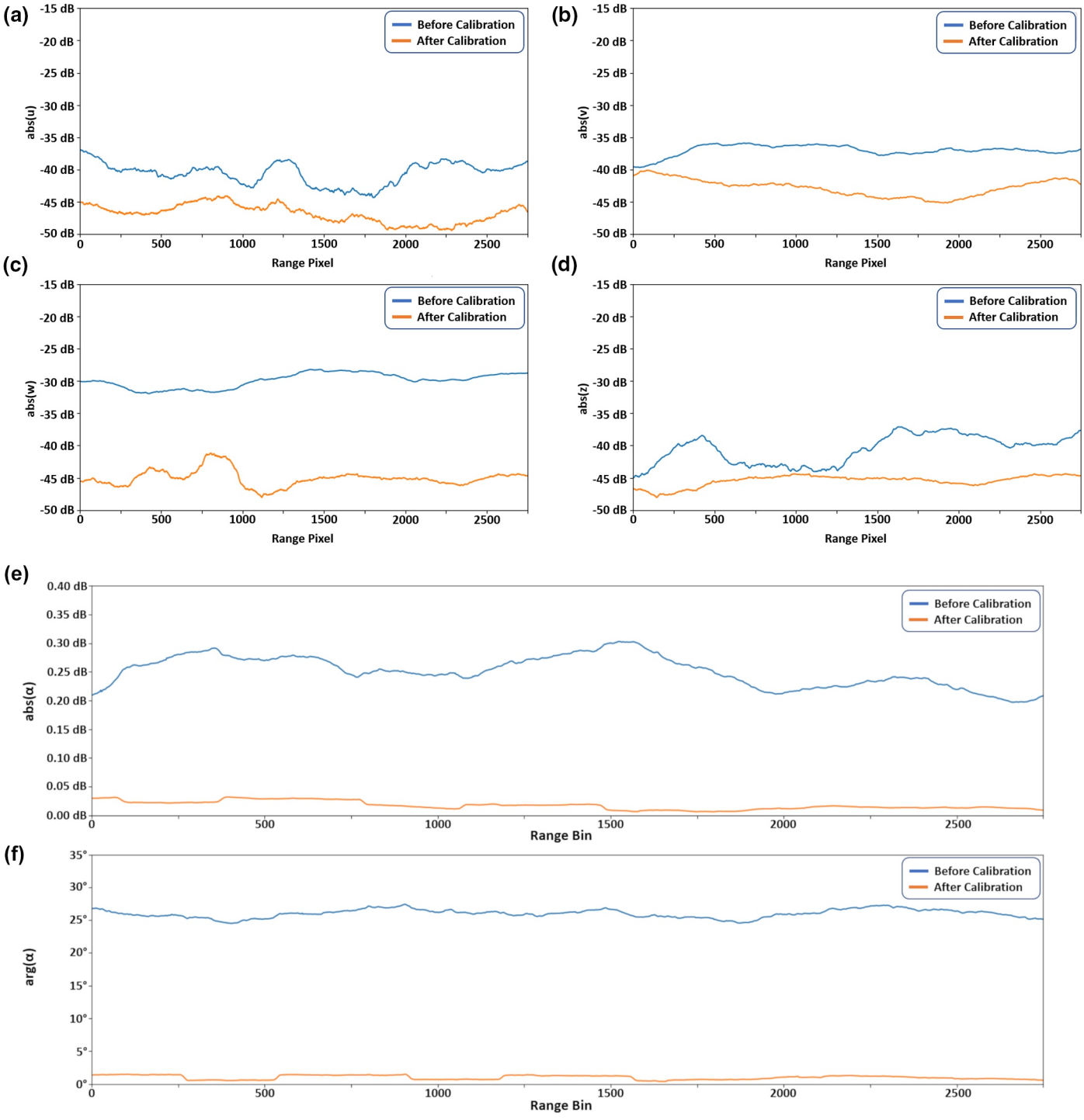

Figure 6. Variation of crosstalk and channel imbalance parameters estimated using Ainsworth's algorithm. The subfigures show the variation of the parameters as follows: (a) abs(u), (b) abs(v), (c) abs(w), (d) abs(z), (e) abs(α), (f) arg(α) All the crosstalk parameters and the channel imbalance parameter have reduced after performing calibration.

The polarimetric signatures after the crosstalk and channel imbalance calibration have been shown in Figures 2c and 2f. It can be observed that the distortions of both co-pol and cross-pol signatures have been reduced. After performing the calibration, similar improvements have been observed in the signatures of other corner reflectors containing some distortions.

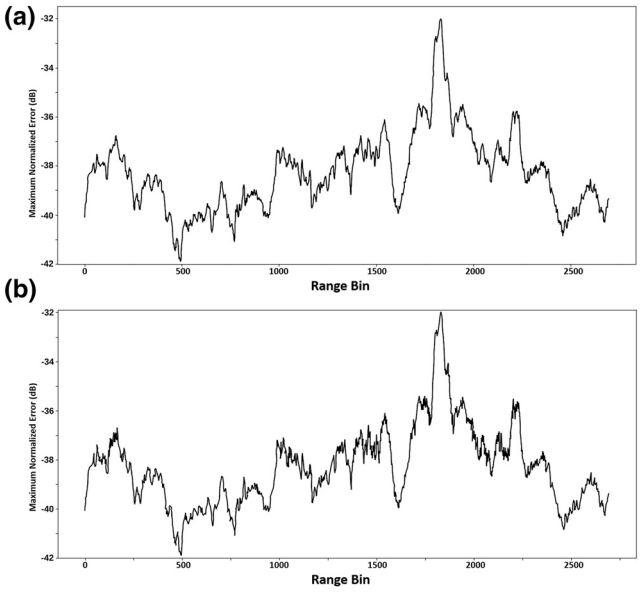

Figure 7. Variation of MNE (a) after calibration using Ainsworth's algorithm, (b) after calibration using proposed algorithm. MNE, maximum normalized error.

The variation of MNE in range direction estimated after the crosstalk calibration is shown in Figure 7a. The MNE highly varied between −32 and −42 dB and reaches maxima near range pixel 1,900. Except for the close neighborhood of the maxima, MNE is below −35 dB in the rest of the range bins.

The histogram of the cross-pol SNR is shown in Figure 8. The histogram of the cross-pol SNR closely follows the normal distribution. After the calibration, the mode has increased to slightly over 8 dB from 6 dB before the calibration.

From Figure 9, it can be observed that the surface scattering is the most dominant scattering having the maximum contribution from the low entropy surface scattering. Consequently, the medium entropy surface scattering and has been significantly reduced. The multiple scattering is higher than the scenario before the calibration which might be related to the rocky patches as discussed earlier. However, the double bounce scattering in the case of Ainsworth's calibration is comparatively lower than that of Quegan's calibration. Interestingly, the anisotropic scattering, in this case, is nearly nonexistent which correctly depicts the characteristics of the surface. Thus, the quality of calibration by Ainsworth's algorithm is better than that of Quegan's algorithm.

4.4. Estimates of Proposed Algorithm

The proposed algorithm adopts a hybrid approach using both Quegan's algorithm and Ainsworth's algorithm to improve the computational efficiency while maintaining the quality of calibration similar to Ainsworth's algorithm. Hence the performance of this algorithm has been evaluated through the following results.

The MNE after the calibration using this method follows a similar pattern to that of Ainsworth's algorithm as it can be observed in Figure 7b. However, some minor differences can be observed approximately in the range of −36 to −39 dB which might be attributed to the cases where the solutions provided by Quegan's algorithm are acceptable. However, the trend is similar to Ainsworth's algorithm in the rest of the cases as the algorithm falls back to Ainsworth's algorithm in case Quegan's estimate is not adequate.

Similar to the MNE, the cross-pol SNR in Figure 10 does not differ significantly from the cross-pol SNR estimates of the data calibrated using Ainsworth's algorithm. Interestingly, the median of the SNR, in this case, has decreased by 0.003 dB from Ainsworth's algorithm. This minute reduction in cross-pol SNR might be attributed to the cases where Quegan's solution has been accepted.

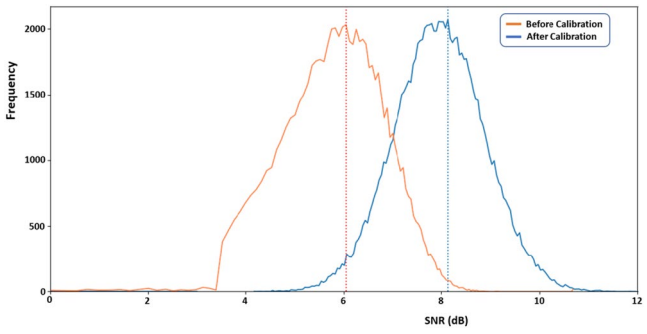

Figure 8. Histogram of cross-pol SNR before and after Ainsworth's crosstalk calibration.

The intended objective of the proposed algorithm is to reduce the high computational cost caused by the iterative construct of Ainsworth's algorithm without harming the accuracy. Therefore, the computational costs of the proposed algorithm have been monitored in terms of the iterations computed for each pixel. The frequency of iterations observed for 1 million pixels (1000 × 1000 subset image) has been shown in Figure 11. Iteration 6 has the highest frequency, that is in most cases, Ainsworth's algorithm inside the proposed algorithm converges with six iterations. The frequencies of iterations steadily decrease after that. The frequency of the 16^{th} iteration is not zero. It indicates that there might be a few instances where the algorithm did not converge up to the expected precision. The frequencies of the initial few iterations are comparatively low since Ainsworth's algorithm initializes with the crosstalk parameters set to zero, that is it is assumed that crosstalk is not present in the data set. Consequently, the algorithm requires a few iterations before it converges.

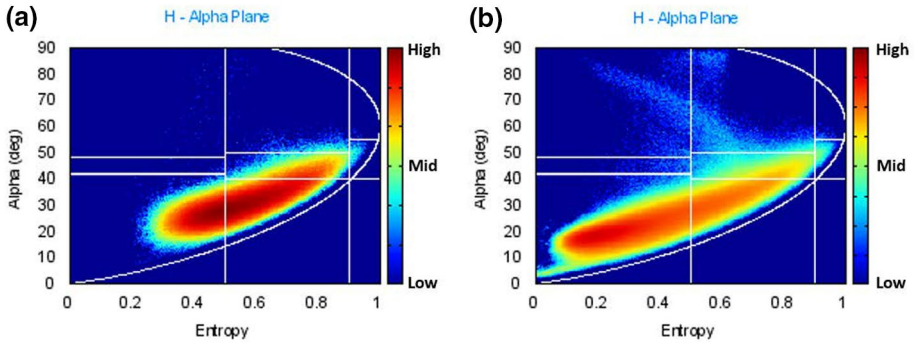

Figure 9. H-α Plane, (a) Before Crosstalk Calibration, (b) After calibration using Ainsworth's algorithm.

Here, zero iteration depicts the cases where the algorithm directly accepted Quegan's solutions. Evidently, in the case of 135.57×10^3 pixels out of 10^6 pixels, the algorithm found the solution of Quegan's estimations to be suitable. Therefore, the iterative computations have been avoided for nearly 13.6% cases.

4.5. Effect of Calibration on Roll Invariant Parameters

The entropy (H) and scattering angle (α) from the H-α decomposition have been observed at the corner reflector points before and after the calibration as these parameters are influenced by the presence of crosstalk. Theoretically, the triangular trihedral corner reflectors depict odd bounce scattering, therefore the value of entropy and scattering angle ideally should be very low in the corner reflector points. However, these two parameters potentially increase in the presence of crosstalk. Consequently, calibration should rectify these anomalies by reducing crosstalk. The changes observed in the value of H and before and after crosstalk calibration for all algorithms are shown in Figure 12. Here, the improved Quegan's algorithm stands for Quegan's algorithm with the cross channel imbalance factor. It can be observed that both the entropy and scattering angle have consistently decreased after each method. Ainsworth's algorithm performs better in terms of reducing these parameters. Expectedly, Quegan's algorithm and Ainsworth's algorithm performs nearly the same as the cross-channel noise imbalance is negligible as per the observations. Similarly, Ainsworth's algorithm and the proposed algorithm performs equally well.

5. Discussion

Comparing the results in Sections 4.2 and 4.3, it is evident that Ainsworth's algorithm is better in terms of minimizing crosstalk than Quegan's algorithm since the residual crosstalk of Ainsworth's algorithm is significantly lower than the residuals of Quegan's algorithm. In some cases, Quegan's algorithm fails to comply with the CEOS cal-val recommendation of maintaining the residual crosstalk below −35 dB (ESA, 2004). In this regard, Ainsworth's algorithm performs well by reducing the residual crosstalk parameters below −40 dB.

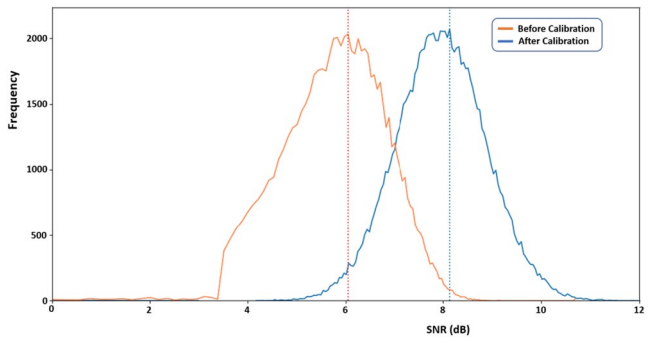

Figure 10. Histogram of cross-pol SNR before and after the crosstalk calibration using the proposed algorithm.

Looking at the polarimetric signatures after the calibrations, it cannot be implied that one algorithm is better at minimizing channel imbalance than the other algorithm, the performance of both the algorithms seems nearly equal. Variations of channel imbalance, however, show that Ainsworth's algorithm is slightly better at minimizing the amplitude of the channel imbalance than Quegan's algorithm. On the contrary, Quegan's algorithm appears to perform better at reducing the phase of the channel imbalance. It can be observed in the plots showing the variations of the phase of the channel imbalance that the estimates by Quegan's algorithm are relatively stable and stays close to the ideal zero value compared to the estimates by Ainsworth's algorithm. However, this difference is negligible.

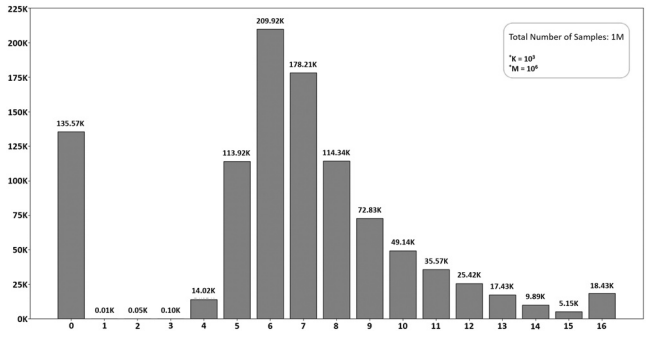

Figure 11. Computational costs of the proposed algorithm observed for 10^6 pixels. Frequencies of each iteration has been shown on the top of each bar.

The accuracies of these algorithms can be better compared in terms of MNE and cross-pol SNR as these metrics adequately represent the actual data quality. According to Wang et al. (2011), −20 dB of MNE translates into −26 dB of crosstalk and the recommended value of MNE is −25 dB. On the contrary, the recommended threshold for the crosstalk is −35 dB (ESA, 2004). Therefore, the threshold for MNE has been set to −30 dB for this study. After performing the calibrations, it is evident from the plots of MNE that the MNE of the data calibrated using Ainsworth's algorithm is significantly lower than the MNE of the data calibrated using Quegan's algorithm. Since MNE is a metric of noise, it can be deduced that Ainsworth's algorithm is better at minimizing the noise present in the data than Quegan's algorithm. On the contrary, cross-pol SNR provides information regarding the useful information content relative to the noise present in the data, in brief, it signifies the quality of the data. The estimated cross-pol SNR after the calibration using Ainsworth's algorithm is higher than the cross-pol SNR estimated after the calibration using Quegan's algorithm. Therefore, concerning the accuracy, Ainsworth's algorithm is better in terms of both the data quality metrics compared to Quegan's algorithm.

In contrast to Quegan's algorithm, the improved Quegan's algorithm considers the possibility of cross-channel noise imbalance. This imbalance is typically sensor-specific (Kimura et al., 2004). According to Hensley et al. (2008), the UAVSAR instrument is well calibrated at the hardware level, and the transceiver module for each band is different. Therefore, the presence of cross-channel noise imbalance is either not present or

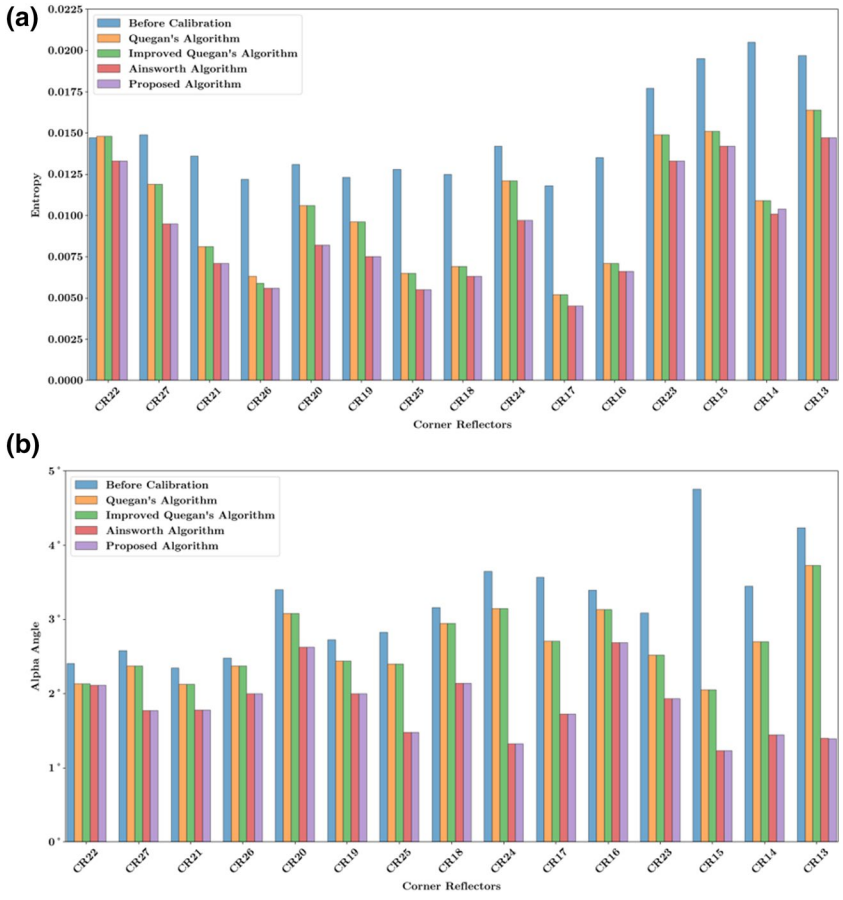

Figure 12. Effect of crosstalk calibration using different algorithms on (a) entropy and (b) scattering angle. Both scattering angle and alpha have reduced due to calibration.

negligible. The estimated value of cross-channel noise imbalance being close to the ideal value of 1 further supports the claim. Expectedly, in this case, hardly any improvements have been observed in case of the improved Quegan's algorithm in contrast to Quegan's algorithm.

POA shift is mainly caused by topographic variations. Referring to the discussion regarding the description of the study area in Section 3, the topographic variation in the study is known to be significantly low. Consequently, the effect of POA shift is also expected to be low. However, small changes in the scattering pattern have been observed by means of decomposition modeling before and after POA shift correction. The volume scattering has been reduced in some places as presented in Section 6, which shows the effectiveness of POA shift compensation.

The proposed algorithm aims to address the high computational cost incurred by the intensive iterative calculations of Ainsworth's algorithm while preserving its accuracy. As per the observations in Section 4.4, the proposed algorithm has avoided iterative computation in 13.6% cases. However, it may vary depending upon the data. In the best-case scenario, the algorithm will accept Quegan's solution in all the cases. Consequently, the complexity of the algorithm will be exactly the same as Quegan's algorithm. Let's assume T_q represents the average time required to estimate the crosstalk parameters for a single pixel using Quegan's algorithm and T_a represents the average time required by a single iteration of Ainsworth's algorithm while estimating the crosstalk parameter for a single pixel. If T represents the average time required to estimate crosstalk parameters by the proposed algorithm for a single pixel then in the best-case, Equation 11 is satisfied where c is the time taken to check whether the solutions meet the accuracy requirement.

$$T = T_q + c \tag{11}$$

In the worst-case, the algorithm accepts only Ainsworth's algorithm's solutions for all the cases. The construct of the algorithm shows that it first computes Quegan's solution then proceeds to compute Ainsworth's solution only if the solutions of Quegan's algorithm do not satisfy the accuracy requirements. Consequently, in the worst-case, both the solutions for both the algorithms will be computed along with the additional checking for accuracy. Thus, in the worst case, T will change as shown in Equation 12 where μ_a is the average number of iterations required in order to obtain the solution of Ainsworth's algorithm. It should be noted that, at worse, μ_a can be equal to the maximum allowed iterations indicating the scenario where all pixels require the maximum number of iterations to converge or do not converge at all. For example, in this case, the maximum value of μ is 16.

$$T = T_q + \mu_a T_a + c \tag{12}$$

However, in the average case, the T will change depending upon the ratio of the pixels where Quegan's solution is accepted with respect to the number of pixels where the solution of Ainsworth's algorithm is accepted. If n is the total number of pixels present in the scene and k is the number of pixels where Quegan's solutions are accepted then T will change as shown in Equation 13.

$$T = T_q + \mu_a T_a \left(\frac{n-k}{n}\right) + c \tag{13}$$

Therefore, the time saved per pixel (ΔT) with respect to Ainsworth's algorithm can be expressed as shown in the Equation 14.

$$\begin{aligned} \Delta T &= \mu_a T_a - \left(T_q + \mu_a T_a \left(\frac{n-k}{n}\right) + c\right) \\ \Rightarrow \Delta T &= \left(\frac{k}{n}\right)\mu_a T_a - T_q - c \\ \Rightarrow \frac{\Delta T}{\mu_a T_a} &= \frac{k}{n} - \frac{T_q + c}{\mu_a T_a} \\ \Rightarrow \frac{\Delta T}{T_A} &\approx \frac{k}{n} : T_A = \mu_a T_a \end{aligned} \tag{14}$$

The term T_A signifies the average time taken by Ainsworth's algorithm to estimate to crosstalk parameters for a single pixel. Clearly, the speedup ($\Delta T/T_A$) solely depends upon the factor $\left(k\ /\ n\right)$. The term T_q can be ignored since it is constant and $T_a \gg T_q$. Similarly, c is also constant and, it can be ignored as well. In this case, $k \approx 135.57 \times 10^3$ and $n = 10^6$, therefore, the speedup is nearly 13.6%. If the terms T_q and c are not ignored the effective speed is expected to be slightly below the 13.6%. It is worth mentioning that this efficiency estimation assumes the Single Instruction Multiple Data (SIMD) computer architecture (Hennessy & Patterson, 2017).

6. Conclusion and Recommendation

The primary objective of this study is to compare the performance of different PolSAR calibration algorithms in terms of accuracy. The study focuses mainly on the two algorithms where the performance of both Quegan's and Ainsworth's algorithm has been assessed using suitable metrics and through different qualitative measures. In addition, the performance of the improved Quegan's algorithm has also been evaluated considering it to be an extension of Quegan's algorithm. Moreover, the effect of POA shift has been estimated and corrected. All the objectives have been completed, and all the research questions have been answered adequately. Furthermore, a modified calibration algorithm has been developed in order to reduce the computational cost.

Quegan's crosstalk algorithm is relatively simple and capable of providing crosstalk estimation quicker than Ainsworth's algorithm. However, in many instances, it fails to reduce the residual crosstalk under the CEOS recommended threshold of −35 dB. Although the cross-pol SNR has improved in case of Quegan's algorithm, the MNE has not been reduced below the limit of −30 dB in all the cases. In contrast, Ainsworth's algorithm not only complied with the CEOS standard and MNE limit but also performed significantly better at minimizing the crosstalk while improving the cross-pol SNR to a higher value than that of Quegan's. Since the cross-channel noise imbalance is negligible in this case, the improved Quegan's algorithm performed nearly the same as Quegan's algorithm. These results unambiguously indicate that Ainsworth's algorithm performs better than Quegan's algorithm in terms of accuracy. Concerning the channel imbalance, both the algorithms perform nearly the same, Ainsworth's algorithm is slightly advantageous, as the reduction of the entropy and scattering angle is relatively higher for this algorithm.

POA shift compensation for this particular study area was not significantly effective due to lack of POA shift attributing to the low topographic variations in the area. However, this does not signify that POA shift correction is unnecessary in all possible scenarios. This procedure necessarily corrects the discrepancies in the scattering pattern incurred by the POA shift if any such anomaly exists. Moreover, the procedure is relatively simple regarding the computation. Therefore, incorporating the POA shift with PolSAR calibration makes the entire process more robust and effective.

The modified algorithm aims to improve the computational efficiency without reducing the accuracy of the estimation. This study successfully demonstrated the gain in the computational efficiency of this algorithm. However, there is no strict lower bound for the improvement in efficiency, which implies that it should perform equally or better than Ainsworth's algorithm.

In essence, Ainsworth's algorithm is equivalent to or better than Quegan's algorithm in every metric with the cost of lower computational efficiency. The use of the proposed algorithm can partly address the higher computational cost. POA shift correction along with the PolSAR calibration reduces most of the potential discrepancies which might be present in the PolSAR data revealing right scattering pattern.

6.1. Recommendation

Based on the results and the discussion, it is evident that this research is based on a single airborne quad-pol SAR data set. Therefore, the findings of this research should be rigorously verified on more datasets to further improve the reliability of the findings. This study can be further extended for the spaceborne SAR data and data acquired in different polarization modes such as dual-pol data set.

Also, we observed nonconvergent behavior in 53 pixels where the matrix is becoming singular. Moreover, for other 164 pixels, the matrix is becoming nearly singular. The solution is thus extremely slow to converge. Moreover, we found that these pixels are scattered throughout the data scene that is not concentrated at a particular region. Furthermore, the number of pixels where the algorithm stops or does not converge (due to the iteration limit) is very low. As an alternative, we strongly recommend that the occurrence of these anomalous pixels can be reduced by optimizing the window size during the computation of covariance matrix. We also suggest another approximate solution in which the focus could be to calculate the calibration parameters of the pixels from the neighboring pixels as a future work.

Appendix A

Additional Corrections

After crosstalk and channel imbalance correction PolSAR data are generally considered to be sufficiently calibrated. However, discrepancies due other factors such as POA shift and Faraday rotation may still be present in the data set. Therefore, the data set should be further refined to reduce these effects. In case of the spaceborne SAR, Faraday rotation due to the presence of ionoshpere can distort the polarisation of transmitting and receiving radar signal. Freeman (2004) evaluated several well-known method to estimate and reduce the effect of Faraday rotation. However, this effect has not been considered in this study as the experiment has been performed on airborene SAR data as stated in Section 3.

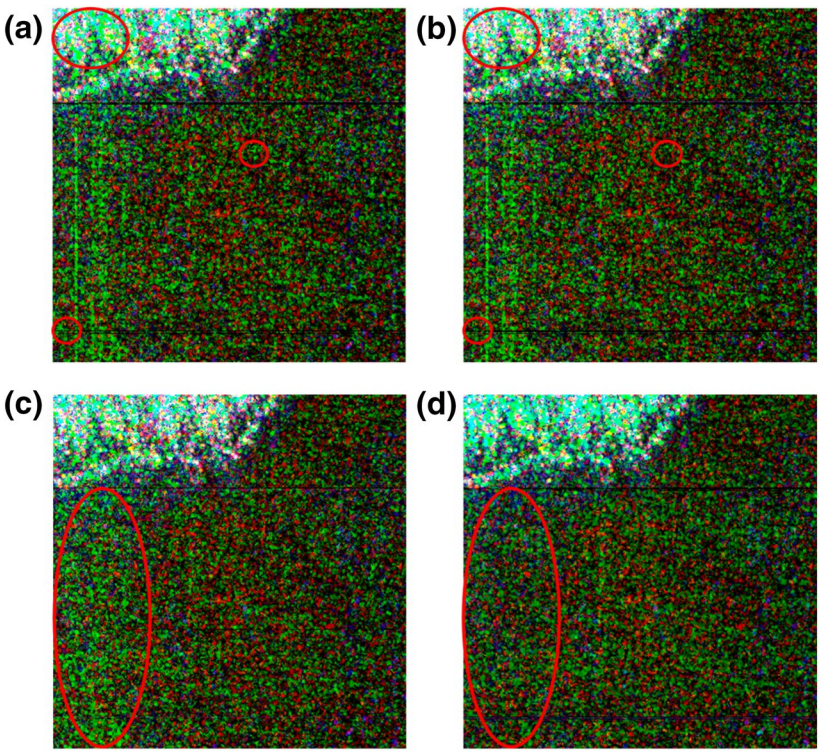

Figure A1. The scattering patterns in the Y4R RGB composite of a small patch. (a) scattering pattern after applying Quegan's algorithm, (b) scattering pattern after applying POA shift correction on the patch calibrated using Quegan's algorithm, (c) scattering pattern after applying Ainsworth's algorithm, (d) scattering pattern after applying POA shift correction on the patch calibrated using Ainsworth's algorithm. Here, Red signifies double bounce scattering, Green signifies volume scattering and blue signifies surface scattering. The respective encircled areas in red are highlighting the changes in the scattering pattern.

Correction of POA Shift

The variation in the azimuthal slope causes rotation of polarisation orientation with respect to the line of sight of the signal (Pottier et al., 1999). Lee et al. (2000) evaluated three major approaches to estimate and correct POA shift and found the circular polarisation based POA shift estimation method proposed by Pottier et al. (1999) to be most reliable. Therefore, in this research, the circular polarisation based POA shift estimation method has been used. According to Lee et al. (2003), the polarisation orientation angle (ψ) can be estimated from the observed scattering matrix ($\tilde{S}$) using the Equations 15a and 15b. After POA shift compensation, the corrected scattering matrix (S) can obtained using the Equation 15c

$$\psi = \begin{cases} \eta & : \ \eta \le \dfrac{\pi}{4} \\ \eta - \dfrac{\pi}{2} & : \ \eta > \dfrac{\pi}{4} \end{cases} \tag{15a}$$

$$\eta = \frac{1}{4}\left[\tan^{-1}\left(\frac{-4\Re\left(\left\langle s_{hv}\left(s_{hh}-s_{hh}\right)\right\rangle\right)}{4\left\langle\left|s_{hv}\right|^2\right\rangle-\left\langle\left|s_{hh}-s_{vv}\right|^2\right\rangle}\right)+\pi\right] : \tan^{-1} \mid \mathbb{R} \rightarrow \left[-\pi,\pi\right] \tag{15b}$$

$$\underbrace{\begin{bmatrix} s_{hh} & s_{hv} \\ s_{vh} & s_{vv} \end{bmatrix}}_{S} = \underbrace{\begin{bmatrix} \cos\psi & \sin\psi \\ -\sin\psi & \cos\psi \end{bmatrix}}_{\rho} \underbrace{\begin{bmatrix} \tilde{s}_{hh} & \tilde{s}_{hv} \\ \tilde{s}_{vh} & \tilde{s}_{vv} \end{bmatrix}}_{\tilde{S}} \underbrace{\begin{bmatrix} \cos\psi & -\sin\psi \\ \sin\psi & \cos\psi \end{bmatrix}}_{\rho^T} \tag{15c}$$

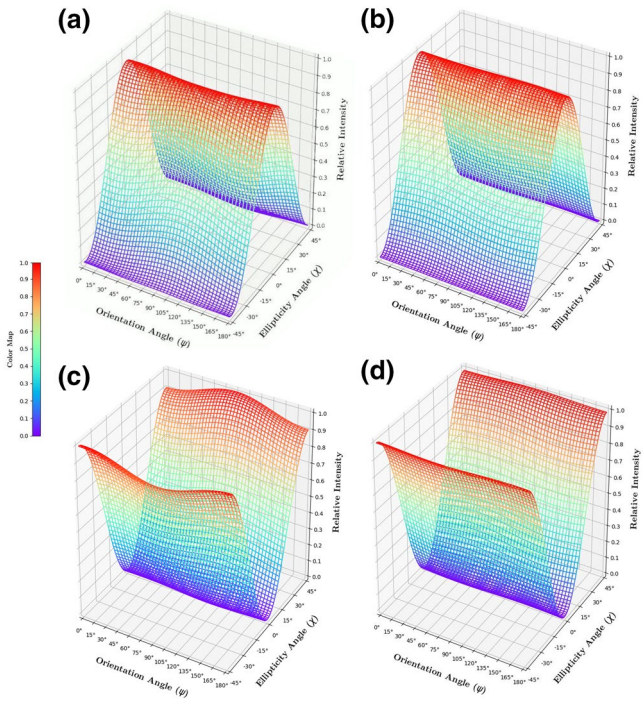

Figure B1. Polarimetric signatures of corner reflector 24. Co-pol signatures are shown in top row, cross-pol signatures are shown in the bottom row. (a and c) are the signatures before calibration, (b and d) are signatures after calibration using our proposed algorithm.

Effect of POA Shift Compensation

In general, the presence of POA shift causes overestimation of volume scattering and underestimation of even bounce scattering. POA shift correction has been performed after the crosstalk calibration by both Quegan's algorithm and Ainsworth's algorithm. In Figure A1, the scattering patterns of a patch calibrated using Quegan's algorithm have been shown before and after performing the POA shift compensation (Figure B1).

It can be observed that in the encircled areas volume scattering has decreased which indicates the changes regarding the POA shift correction. However, these changes are relatively small, which is justifiable as the topographic variations in the study area are negligible. Similar behavior can be observed in Figure 31 in the case of POA shift correction after the calibration using Ainsworth's algorithm. In Figure 12a, the presence of significant volume scattering can be observed which has been further reduced in Figure 12b as a result of POA shift compensation. However, in both cases, the changes in the double bounce scattering due to POA shift have not been observed since the calibrated scenes hardly show any double-bounce scattering.

Data Availability Statement

UAVSAR polarimetric data set (NASA/JPL, 2013) supporting this research are freely accessible at UAVSAR Data Repository (ASA/JPLNASA/JPL, 2020).

Acknowledgments
Under the NASA–ISRO Synthetic Aperture Radar (NISAR) technological development initiative, project funding from https://www.isro.gov.in/ISRO, Govt. of India has been acknowledged. We also thank https://uavsar.jpl.nasa.gov/UAVSAR Team, NASA/JPL, 2020, for providing the UAVSAR data set.

References

Ainsworth, T. L., Ferro-Famil, L., & Jong-Sen, L. (2006). Orientation angle preserving a posteriori polarimetric SAR calibration. *IEEE Transactions on Geoscience and Remote Sensing*, *44*(4), 994–1003. https://doi.org/10.1109/TGRS.2005.862508

Ainsworth, T. L., & Lee, J.-S. (2001). A new method for a posteriori polarimetric SAR Calibration. In *Igarss 2001. Scanning the present and resolving the future proceedings IEEE 2001 international geoscience and remote sensing symposium (cat. no.01ch37217)* (Vol. *1*, pp. 420–422). Sydney: IEEE. Retrieved from http://ieeexplore.ieee.org/document/976177/10.1109/IGARSS.2001.976177

Al-kahachi, N. (2014). Polarimetric cross-talk in SAR system induced by Antenna Cross–Pol Pattern. *European Conference on Synthetic Aperture Radar* (pp. 1365–1368).

Babu, A., Kumar, S., & Agrawal, S. (2019). Polarimetric calibration of RISAT-1 compact-pol data. *IEEE Journal of Selected Topics in Applied Earth Observations and Remote Sensing*, *12*(10), 3731–3736. https://doi.org/10.1109/jstars.2019.2932019

Baffelli, S., Frey, O., Werner, C., & Hajnsek, I. (2018). Polarimetric calibration of the Ku-Band advanced polarimetric radar interferometer. *IEEE Transactions on Geoscience and Remote Sensing*, *56*(4), 2295–2311. https://doi.org/10.1109/TGRS.2017.2778049

Chang, Y., Li, P., Yang, J., Zhao, J., Zhao, L., & Shi, L. (2018). Polarimetric calibration and quality assessment of the GF-3 satellite images. *Sensors (Switzerland)*, *18*(2), 1–12. https://doi.org/10.3390/s18020403

Clifford, P. (1985). The international vocabulary of basic and general terms in metrology. *Measurement*, *3*(2), 72–76. https://doi.org/10.1016/0263-2241(85)90006-5

Cloude, S. R. (2009). *Polarisation: Applications in remote sensing* (1st ed.). Chippenham, Wiltshire: Oxford University Press. https://doi.org/10.1093/acprof:oso/9780199569731.001.0001

Doerry, A. W., & Bickel, D. L. (2018). Measuring channel balance in multi-channel radar receivers. *Proc. SPIE 10633, Radar Sensor Technology XXII, 106331A*. https://doi.org/10.1117/12.2303455

Doring, B. J., Looser, P., Jirousek, M., & Schwerdt, M. (2011). Point target correction coefficients for absolute SAR calibration. In *2011 IEEE international instrumentation and measurement technology conference* (pp. 1–6). IEEE. Retrieved from http://ieeexplore.ieee.org/document/5944111/10.1109/IMTC.2011.5944111

El-Darymli, K., McGuire, P., Gill, E., Power, D., & Moloney, C. (2014). Understanding the significance of radiometric calibration for synthetic aperture radar imagery. In *2014 IEEE 27th Canadian Conference on Electrical and Computer Engineering (CCECE)* (pp. 1–6). IEEE. Retrieved from http://ieeexplore.ieee.org/document/6901104/10.1109/CCECE.2014.6901104

ESA. (2004). *Recommendation at CEOS CAL/VAL 2004*. Retrieved 2019-02-23, from http://earth.esa.int/workshops/ceos_sar_2004/recommendation_at_ceos_cal.html

Fore, A. G., Chapman, B., Hensley, S., Michel, T., & Muellerschoen, R. (2009). *UAVSAR polarimetric calibration (Tech. Rep.)*. Pasadena, CA: Jet Propulsion Laboratory, NASA. Retrieved from http://uavsar.jpl.nasa

Fore, A. G., Chapman, B. D., Hawkins, B. P., Hensley, S., Jones, C. E., Michel, T. R., & Muellerschoen, R. J. (2015). UAVSAR Polarimetric Calibration. *IEEE Transactions on Geoscience and Remote Sensing*, *53*(6), 3481–3491. https://doi.org/10.1109/TGRS.2014.2377637

Freeman, A. (2004). Calibration of linearly polarized polarimetric SAR data subject to Faraday rotation. *IEEE Transactions on Geoscience and Remote Sensing*, *42*(8), 1617–1624. https://doi.org/10.1109/TGRS.2004.830161

Freeman, A., van Zyl, J., Klein, J. D., Zebker, H. A., & Shen, Y. (1992). Calibration of Stokes and scattering matrix format polarimetric SAR data. *IEEE Transactions on Geoscience and Remote Sensing*, *30*(3), 531–539. https://doi.org/10.1109/36.142931

Gibbs, Y. (2017). *NASA dryden fact sheets - the dry lakes (Tech. Rep.). NASA*. Retrieved from https://www.nasa.gov/centers/armstrong/news/FactSheets/FS-086-DFRC.html

Gray, A., Vachon, P., Livingstone, C., & Lukowski, T. (1990). Synthetic aperture radar calibration using reference reflectors. *IEEE Transactions on Geoscience and Remote Sensing*, *28*(3), 374–383. https://doi.org/10.1109/36.54363

Hennessy, J., & Patterson, D. (2017). Data-Level parallelism in vector, SIMD, and GPU architectures. In *Computer architecture* (6th ed., pp. 282–357). Cambridge, MA: Elsevier Inc. Retrieved from https://www.elsevier.com/books/computer-architecture/hennessy/978-0-12-811905-1

Hensley, S., Wheeler, K., Sadowy, G., Jones, C., Shaffer, S., Zebker, H., et al. (2008, may). The UAVSAR instrument: Description and first results. In *2008 IEEE Radar Conference* (pp. 1–6). IEEE. Retrieved from http://ieeexplore.ieee.org/document/4720722/10.1109/RADAR.2008.4720722

Kimura, H., Mizuno, T., Papathanassiou, K. P., & Hajnsek, I. (2004). Improvement of polarimetric SAR calibration based on the Quegan algorithm. In *IEEE International Geoscience and Remote Sensing Symposium, 2004. IGARSS '04. Proceedings*. 2004 (Vol. *1*, pp. 184–187). IEEE. Retrieved from http://ieeexplore.ieee.org/document/1368990/10.1109/IGARSS.2004.1368990

Lee, J.-S., & Ainsworth, T. L. (2011). The effect of orientation angle compensation on coherency matrix and polarimetric target decompositions. *IEEE Transactions on Geoscience and Remote Sensing*, *49*(1), 53–64. https://doi.org/10.1109/tgrs.2010.2048333

Lee, J.-S., Ainsworth, T. L., & Schuler, D. L. (2003). *A review of polarization orientation estimation from polarimetric SAR data*. Frascati: European Space Agency. Retrieved from http://adsbit.harvard.edu//full/2003ESASP.529E...3L/0000003.001.html

Lee, J.-S., Ainsworth, T. L., & Wang, Y. (2018). Polarization orientation angle and polarimetric SAR scattering characteristics of steep terrain. *IEEE Transactions on Geoscience and Remote Sensing*, *56*(12), 7272–7281. https://doi.org/10.1109/TGRS.2018.2849931

Lee, J.-S., Schuler, D. L., & Ainsworth, T. L. (2000). Polarimetric SAR data compensation for terrain azimuth slope variation. *IEEE Transactions on Geoscience and Remote Sensing*, *38*(5), 2153–2163. https://doi.org/10.1109/36.868874

Liu, G., Zhang, J., Zhang, X., & Wang, G. (2016). Impact of cross-talk contamination and channel imbalance for marine target surveillance. In *2016 CIE International Conference On Radar (RADAR)*. IEEE. Retrieved from https://doi.org/10.1109/radar.2016.8059384

Maiti, A. (2019). *Polarimetric calibration of sar data using manmade point targets and uniformly distributed natural targetsFaculty of Geo-Information Science and Earth Observation*. Retrieved from https://library.itc.utwente.nl/papers_2019/msc/gfm/maiti.pdf

Meyer, R. W., & Bowers, J. C. (2012). *Flood-prone areas and waterways, Edwards air force base (Tech. Rep.)*, Sacramento, CA: USGS. Retrieved from https://pubs.usgs.gov/of/2000/ofr00183/ofr00183.pdf

Moreira, A., Prats-Iraola, P., Younis, M., Krieger, G., Hajnsek, I., & Papathanassiou, K. P. (2013). A tutorial on synthetic aperture radar. *IEEE Geoscience and Remote Sensing Magazine*, *1*(1), 6–43. https://doi.org/10.1109/MGRS.2013.2248301

Muellerschoen, R. (2018). *Calibration–UAVSAR*. Retrieved from https://uavsar.jpl.nasa.gov/cgi-bin/calibration.pl

NASA/JPL. (2013). *UAVSAR PolSAR. NASA Alaska satellite facility DAAC*. Retrieved from https://www.asf.alaska.edu/data-sets/sar-data-sets/uavsar/10.5067/7PEQV8SVR4DM

NASA/JPL. (2020). Data Repository–UAVSAR. *JPL, NASA*. Retrieved from https://uavsar.jpl.nasa.gov/cgi-bin/data.pl

Pottier, E., Schuler, D. L., Lee, J.-S., & Ainsworth, T. L. (1999). Estimation of the terrain surface azimuthal/range slopes using polarimetric decomposition of POLSAR data. In *IEEE 1999 International Geoscience and Remote Sensing Symposium. IGARSS'99 (cat. no.99ch36293)* (Vol. *4*, pp. 2212–2214). IEEE. Retrieved from http://ieeexplore.ieee.org/document/775080/10.1109/IGARSS.1999.775080

Quegan, S. (1994). A unified algorithm for phase and cross-talk calibration of polarimetric data–theory and observations. *IEEE Transactions on Geoscience and Remote Sensing*, *32*(1), 89–99. https://doi.org/10.1109/36.285192

Rosen, P., Hensley, S., Wheeler, K., Sadowy, G., Miller, T., Shaffer, S., et al. (2006). UAVSAR: A new NASA airborne SAR system for science and technology research. In *2006 IEEE Conference on Radar* (pp. 22–29). Verona, NY: IEEE. Retrieved from http://ieeexplore.ieee.org/document/1631770/10.1109/RADAR.2006.1631770

Sato, D., Watanabe, T., Yamada, H., & Yamaguchi, Y. (2013). Comparison of model-based polarimetric decomposition algorithms. In *Asia-pacific conference on synthetic aperture radar (apsar) conference proceedings of 2013*. (pp. 346–349). Tsukuba, Japan: IEEE.

Shimada, M. (2011). Model-Based polarimetric SAR calibration method using forest and surface-scattering targets. *IEEE Transactions on Geoscience and Remote Sensing*, *49*(5), 1712–1733.Retrieved from http://ieeexplore.ieee.org/document/5682040/10.1109/TGRS.2010.2090046

Shukla, S., & Kumar, S. (2018). Effect of polarization orientation angle compensation on airborne l-band uavsar data for the Munich area, Germany. *Eusar 2018; 12th European Conference on Synthetic Aperture Radar*. (pp. 1–6).

Skriver, H., Dierking, W., Gudmandsen, P., Le Toan, T., Moreira, A., Papathanassiou, K., & Quegan, S. (2003). Applications of synthetic aperture radar polarimetry (72(529), pp. 11–16).European Space Agency, (Special Publication) ESA SP. Retrieved from http://linkinghub.elsevier.com/retrieve/pii/S0024320503000699

van Zyl, J., & Kim, Y. (2011). *Synthetic aperture radar Polarimetry*. Hoboken, NJ, USA: John Wiley & Sons, Inc. Retrieved from http://books.google.com/books?id=9XLR9Sm1FJ4C

Villano, M., & Papathanassiou, K. P. (2013). SNR and noise variance estimation in polarimetric SAR data. In *Esa polinsar workshop*. Frascati, Italy: ESA. Retrieved from https://elib.dlr.de/83036/

Wang, Y., Ainsworth, T. L., & Lee, J.-S. (2011). Assessment of system polarization quality for polarimetric SAR imagery and target decomposition. *IEEE Transactions on Geoscience and Remote Sensing*, *49*(5), 1755–1771.Retrieved from http://ieeexplore.ieee.org/document/5661826/10.1109/TGRS.2010.2087342